Humate-assisted Synthesis of MoS_2/C Nanocomposites via Co-Precipitation/Calcination Route for High Performance Lithium Ion Batteries

- Qin Geng,
- Xin Tong,
- Gideon Evans Wenya,
- Chao Yang,
- Jide Wang,
- A. S. Maloletnev,
- Zhiming M. Wang &
- Xintai Su

Nanoscale Research Letters **volume 13**, Article number: 129 (2018) Cite this article

- **1841** Accesses
- **13** Citations
- Metricsdetails

Abstract

A facile, cost-effective, non-toxic, and surfactant-free route has been developed to synthesize MoS_2/carbon (MoS_2/C) nanocomposites. Potassium humate consists of a wide variety of oxygen-containing functional groups, which is considered as promising candidates for functionalization of graphene. Using potassium humate as carbon source, two-dimensional MoS_2/C nanosheets with irregular shape were synthesized via a stabilized co-precipitation/calcination process. Electrochemical performance of the samples as an anode of lithium ion battery was measured, demonstrating that the MoS_2/C nanocomposite calcinated at 700 °C (MoS_2/C-700) electrode showed outstanding performance with a high discharge capacity of 554.9 mAh g^{-1} at a current density of 100 mA g^{-1} and the Coulomb efficiency of the sample maintained a high level of approximately 100% after the first 3 cycles. Simultaneously, the MoS_2/C-700 electrode exhibited good cycling stability and rate performance. The success in synthesizing MoS_2/C nanocomposites via co-precipitation/calcination route may pave a new way to realize promising anode materials for high-performance lithium ion batteries.

Background

Due to their high energy density, long cycle life, and environmental friendliness, lithium ion batteries (LIBs) are widely utilized in portable electronic devices [1] (e.g., mobile phones and watches), electric vehicles [2, 3], and renewable energy storage [4,5,6,7,8].

Graphite is the most widely used anode materials in commercial LIBs, benefiting from its low working voltage, good conductivity, and low cost [9,10,11]. However, the characteristic structure of graphite leads to feasible generation of LiC_6, allowing only one lithium ion intercalation in every six carbon atoms which results in a low theoretical specific capacity of 372 mAh g^{-1}, which is far away from the current business requirements [12].

Currently, it is preferred to obtain appropriate electrode materials in LIBs for higher battery capacity, longer cycle life, and better rate capability. Consequently, Li-alloy-based anode materials [13], transition metal oxides [14], oxysalts, and transition metal sulfides [15] are often served as the anode materials in LIBs, since these materials display all the necessary properties for appropriate electrode materials. Among these materials, transition metal sulfides (e.g., CuS_2 [16], WS_2 [17], and MoS_2 [18,19,20] have been an exciting topic in research as they are earth-abundant and show high specific capacity when used as anode materials in LIBs [21]. As a typical representative, MoS_2 has gained a lot of attention due to its particular S-Mo-S layered structure [22], high theoretical specific capacity compared to traditional graphite anode, and there is a transfer reaction of four electrons when used as anode materials in LIBs [23, 24]. In addition, the van der Waals forces between the MoS_2 layers are very weak, allowing lithium-ion diffusion without causing significant volume change [25, 26]. However, MoS_2 is still an unsatisfactory anode material due to its low electrical conductivity, leading to the poor cycling and rate performance [27]. To solve this problem, a number of strategies have been developed to improve its electrical conductivity such as the incorporation of MoS_2 with carbon materials [28,29,30].

To date, a variety of MoS_2/carbon composites have been synthesized as anode materials in LIBs, namely, layered MoS_2/graphene composites [31], MoS_2/C multilayer nanospheres [32], MoS_2-CNT composite [33], multilayered graphene/MoS_2 heterostructures [34], or petal-like MoS_2 nanosheets space-confined in hollow mesoporous carbon spheres [35]. Despite gratifying progress in electrical conductivity, cycling, and rate performance of the electrode, some other conflicts in the synthesis method have persisted. At present, the most commonly used synthetic method is hydrothermal approach followed by an annealing process, which can introduce carbon matrix with some surfactants such as sodium oleate or oleyamine and sulfur element with some L-cysteine in the first procedure. Moreover, expensive and toxic organic reagents were always indispensable and unavoidable during the synthesis process when compared with co-precipitation method. Currently, co-precipitation method is just beginning to gain popularity in the synthesis of inorganic nanostructured materials due to its cost-effective, non-toxic, trustworthy, and stable [36, 37]. To the best of our knowledge, there has been little report on the synthesis of MoS_2/C nanocomposite by co-precipitation/calcination process, especially with potassium humate.

Potassium humate, a sort of aromatic hydroxy carboxylate, which consisted of a wide variety of oxygen-containing functional groups, can be considered as functionalized graphene candidate [38]. In general, a great deal of researches have been made to use potassium humate as carbon source to synthesize carbon materials under extremely harsh conditions [38, 39]. Huang [38] reported that potassium humate can be straightforward carbonization to prepare reduced graphite oxide materials. In this paper,

MoS_2/C nanocomposites were synthesized via a co-precipitation/calcination route, by employing an organic matter (potassium humate) and an inorganic substance ($(NH_4)_6Mo_7O_{24}$) as reagents. The electrochemical performance of the samples as a LIBs anode was measured, and the results showed that the sample calcinated at 700 °C (MoS_2/C-700) exhibited better cycling ability and rate behavior. The discharge capacity of the sample remained at 554.9 mAh g^{-1} after 50 cycles at the current density of 100 mA g^{-1}, which is much better than the other two samples calcinated at 600 °C and 800 °C, respectively. Meanwhile, the as-prepared MoS_2/C-700 displays a comparable electrochemical performance [40, 24].

Methods/Experimental

Potassium humate was obtained from Double Dragons Humic Acid Co., Ltd. Xinjiang (China), and the composition analysis of potassium humate was shown in Additional file 1: Table S1. All of the chemical reagents (except potassium humate) were of pure analytical grade and used without further purification.

Synthesis of MoS_2/C

The precursor was prepared by co-precipitation from $(NH_4)_6Mo_7O_{24}$ and potassium humate in the presence of HNO_3 followed by a freeze-dried process for 2 days. In a typical procedure, 4 g of potassium humate were dissolved in 40 mL of 0.25 M $(NH_4)_6Mo_7O_{24}$ solution. Subsequently, the above-mentioned solution was added dropwise to 100 mL of 0.5 M HNO_3 solution with vigorous magnetic stirring. The duration of the magnetic stirring was for several hours. The lower precipitation was then separated from the mixture solution, freeze-dried, and labeled as Mo-HA precursor. The precursor was mixed with anhydrous Na_2SO_4 (with a proportion of 1:10) and ground in a mortar to form a homogeneous mixture. The mixture was then calcinated at 700 °C for 3 h (with a heating rate of 10 °C min^{-1}) and then naturally cooled down to room temperature. Finally, the products were washed with deionized water and ethanol three times followed by a freeze-dried procedure to obtain the MoS_2/C powder. In parallel, the samples calcinated at 600 and 800 °C were synthesized as well.

Characterization

The surface organic functional groups of potassium humate were measured by Fourier transform spectrophotometer (FT-IR, VERTEX 70, Bruker) with KBr as the reference sample. The structure and morphology of different samples were characterized by X-ray diffraction (XRD, BRUKER D8 Advance) with Cu Kα radiation ($\lambda = 1.54178$ Å), transmission electron microscopy (TEM, Hitachi H-600), high-resolution transmission electron microscopy (HRTEM, JEM-2100F), LEO 1450VP scanning electron microscope (SEM), energy-dispersive X-ray spectrometer (EDX), and X-ray photoelectron spectroscopy (XPS, ESCALAB 250Xi spectrometer). Thermogravimetric analyses (TGA) were conducted on a thermogravimetric analyzer (Netzsch TGA 409). Raman spectrum was carried out on Bruker Senterra with 532 nm wavelength.

Electrochemical Measurements

Electrochemical measurements were performed on coin cells. The working electrodes were fabricated by mixing 80 wt.% of the as-prepared MoS_2/C active materials, 10 wt.% of acetylene black, and 10 wt.% of polyvinylidene fluoride (PVDF) in

N-methyl-2-pyrrolidinone (NMP) solvent to form a homogeneous slurry. The slurry was coated on the copper foil and dried in a vacuum at 110 °C for 12 h. The coin cells were assembled in an argon-filled glovebox. In the measurement, lithium foil was used as the counter electrode and reference electrode, and a polypropylene film (Celgard-2400) was used as a separator. The electrolyte solution was 1 mol L^{-1} $LiPF_6$ in ethylene carbonate (EC), dimethyl carbonate (DMC), and diethyl carbonate (DEC) (EC/DMC/DEC, 1:1:1, volume ratio). The galvanostatic charge-discharge measurements were performed in a potential range of 0.01–3.0 V by using a LAND CT2001A battery testing instrument (Wuhan) at room temperature. Cyclic voltammetry (CV) measurements were performed on an electrochemical work-station (CHI 660D) at a scanning rate of 0.1 mV s^{-1} between 0.01 and 3.0 V.

Results and Discussion

The surface chemistry of potassium humate was studied using FTIR spectrum. In Fig. 1a, the broad peaks centered at 3400 cm^{-1} were ascribed to the stretching vibrations of −OH, −COOH, and H_2O bonds, The peaks at 1627, 1413, and 1050 cm^{-1} were attributed to the stretching vibrations of the −COO groups and −CH, −OH and so on [41], respectively, indicating the rich oxygen-containing functional groups on the surface of pure potassium humate, which is beneficial to complexation reaction or adsorption. TGA curve of the homogeneous mixture of Mo-HA precursor and anhydrous Na_2SO_4 (with a proportion of 1:10) in an argon atmosphere with a heating rate of 10 °C min^{-1} is shown in Fig. 1b. It can be seen that there are three steps of weight loss in the TGA curve. The first weight loss is 1.59% from room temperature to 250 °C, which may be due to decomposition of the water in the surface of the Mo-HA precursors. There are another two consecutive steps of weight loss, with a weight loss of 1.35% from 250 to 500 °C, and a weight loss of 3.17% from 500 to 800 °C, and then the mass remains constant, indicating that the precursor has been decomposed completely at 800 °C. For such a system, we choose those three temperatures for calcination as 600, 700, and 800 °C, denoted as MoS_2/C-600, MoS_2/C-700, and MoS_2/C-800, respectively.

Fig. 1

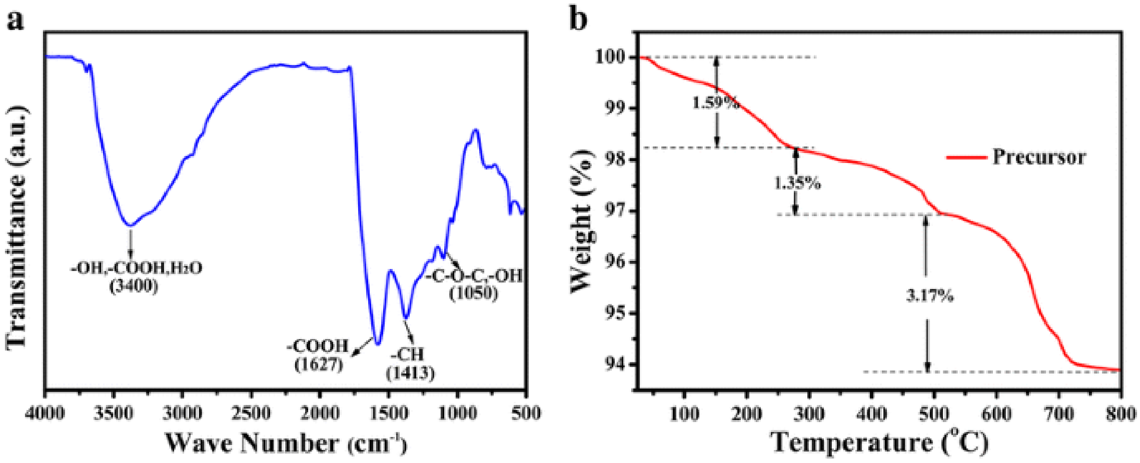

a FT-IR spectra of pure potassium humate. **b** TGA curve of the homogeneous mixture of Mo-HA precursor and anhydrous Na_2SO_4 (with a proportion of 1:10)

Full size image

According to the literature [34], a possible mechanism of the reaction process has been proposed and schematically depicted in Scheme 1. Moreover, the corresponding formulas are listed in Additional file 1: Equations 1–5. In these equations, potassium humate was abbreviated as K-HA. There might be a complexation when potassium humate was dissolved in $(NH_4)_6Mo_7O_{24}$ solution, with the participation of HNO_3 solution, which leads to the generation of Mo-HA. After heating the mixture of the Mo-HA precursor and anhydrous Na_2SO_4 in an argon atmosphere at a relatively high temperature, the Mo-HA precursor would be carbonized to form the intermediate of amorphous carbon, and then the intermediate would reduce anhydrous Na_2SO_4 to generate Na_2S, further hydrolyzed to hydrogen sulfur. Finally, hydrogen sulfur may react with MoO_x, leading to the formation of MoS_2/C nanocomposites.

Scheme 1

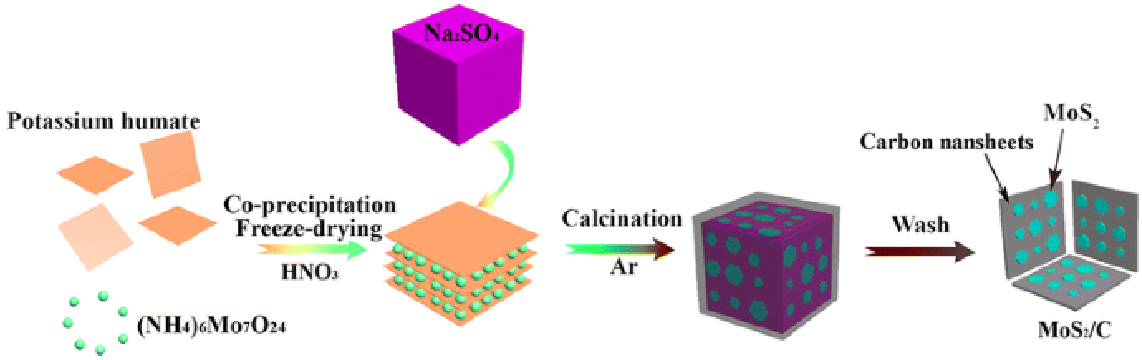

Schematics depicting the fabrication procedure of MoS_2/C nanocomposite

Full size image

Figure 2a–b show the XRD patterns and Raman spectra of the MoS_2/C nanocomposites calcinated at different temperatures. Figure 2a shows that almost all the diffraction peaks of MoS_2/C-600 and MoS_2/C-700 can be well indexed to the hexagonal MoS_2 phase (JCPDS card no. 86-2308), which is consistent with those of previous report [42]. There are still some other peaks mismatching the standard card in the MoS_2/C-800 sample. We speculate that the crystalline of MoS_2/C has been destroyed at high temperature. From the Raman spectra (Fig. 2b), it can be seen that the peaks located in between 379 and 400 cm^{-1} belonged to E^{1}_{2g} (the in-plane displacement of Mo and S atoms) and A_{1g} (out-of-plane symmetric displacement of Mo and S atoms) Raman modes, respectively [24, 43]. The bands appeared at 1347 and 1589 cm^{-1} were the characteristic D- and G-band, and the value of I_D/I_G were 0.96, 0.91, and 0.94 as the temperature goes from 600 to 800 °C. The former corresponds to the amorphous carbon or sp^3-hybridized carbon (D-band), and the latter assigned to the sp^2-hybridized carbon (G-band) [44]. Although there is no great distinction between the degree of graphitization, the MoS_2/C-700 sample is still a little higher than the other two samples to a certain extent, indicating that the carbon in this sample is not only in the form of amorphous carbon, but also some graphitic carbon. Therefore, we focused on the MoS_2/C-700 sample in the following investigations.

Fig. 2

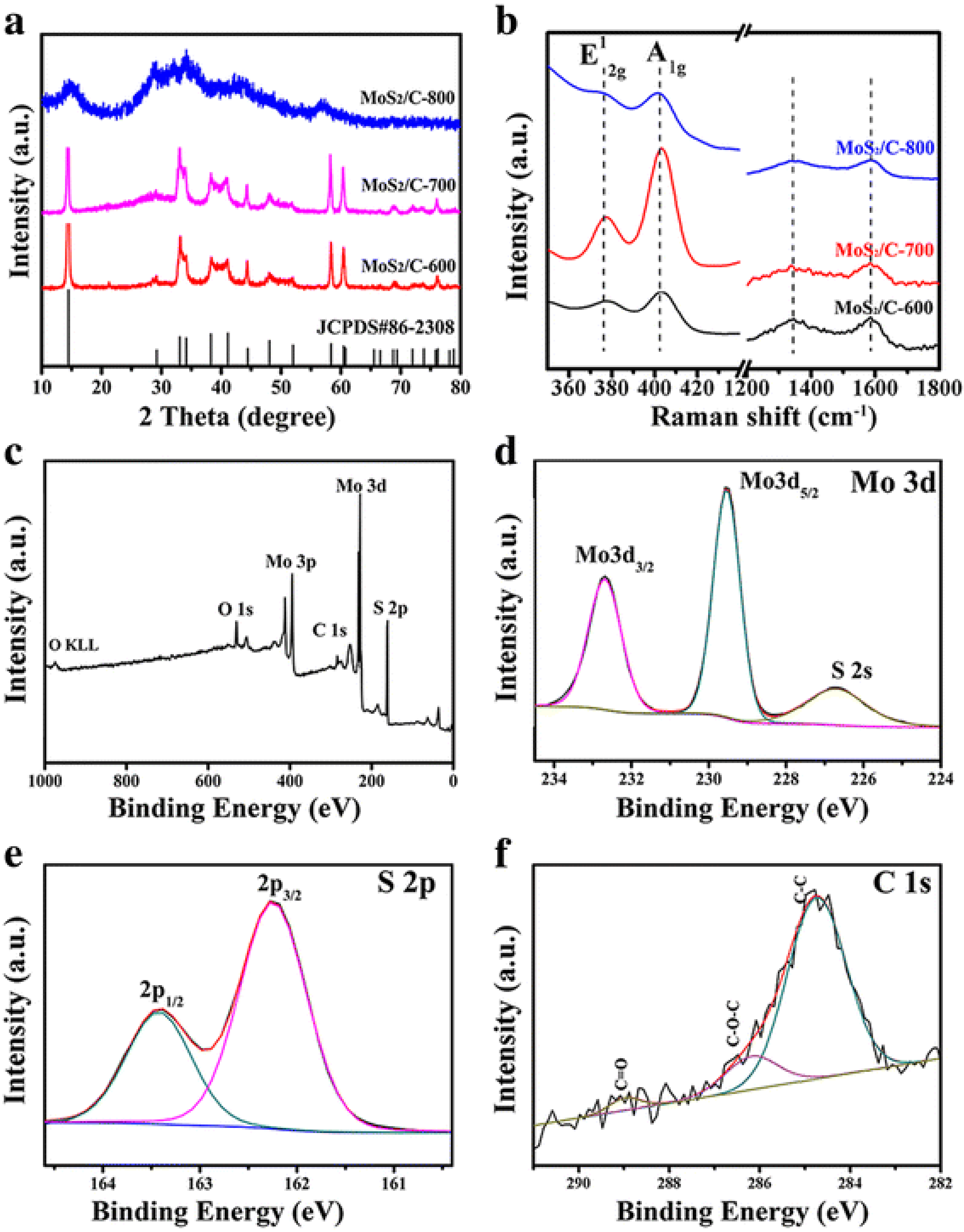

a XRD patterns. **b** Raman spectra of MoS_2/C nanocomposites calcinated at different temperatures. **c** Survey XPS spectra of MoS_2/C-700. **d** High-resolution XPS spectra of Mo 3d. **e** S 2p. **f** C 1 s

Full size image

To further study the chemical composition and chemical bonds of MoS_2/C-700, X-ray photoelectron spectroscopy (XPS) analysis was carried out. The survey XPS spectrum (Fig. 2c–f) reveals the presence of Mo, S, C, and O elements in the MoS_2/C-700 nanocomposite. The high-resolution XPS spectra of Mo 3d and S 2p are shown in Fig. 2d, e, respectively. The peaks at 229.4 and 232.6 eV are assigned to the Mo $3d_{5/2}$ and Mo $3d_{3/2}$, confirming the existence of Mo in MoS_2/C-700 [45, 46]. The presence of another XPS peak at 226.5 eV is indexed to S 2 s, which is resulted from the surface of the MoS_2/C-700 [47]. Moreover, the XPS peaks at 162.3 and 163.4 eV in S 2p spectra are characteristic peaks of the S $2p_{3/2}$ and S $2p_{1/2}$ of MoS_2, respectively. Figure 2f shows that the C1 s spectrum can be divided into three peaks, denoted as C–C, C–O, and C=O groups, respectively.

The EDX spectrum indicates that the sample calcinated at 700 °C contains Mo, S, and C elements, as shown in Fig. 3a. Figure 3b, c show the SEM images of the sample of MoS_2/C-700. For comparison, the SEM images of MoS_2/C-600 nanocomposite and MoS_2/C-800 nanocomposite were also shown in Additional file 1: Figure S1. In order to explore the corresponding element distribution in the sample of MoS_2/C-700, the corresponding elemental mapping analysis were carried out. As shown in Fig. 4a–d, the elemental mapping images of MoS_2/C-700 demonstrated the uniform distribution of Mo, S, and C all over the MoS_2/C-700 nanocomposite, which is consistent with the EDX and XPS results.

Fig. 3

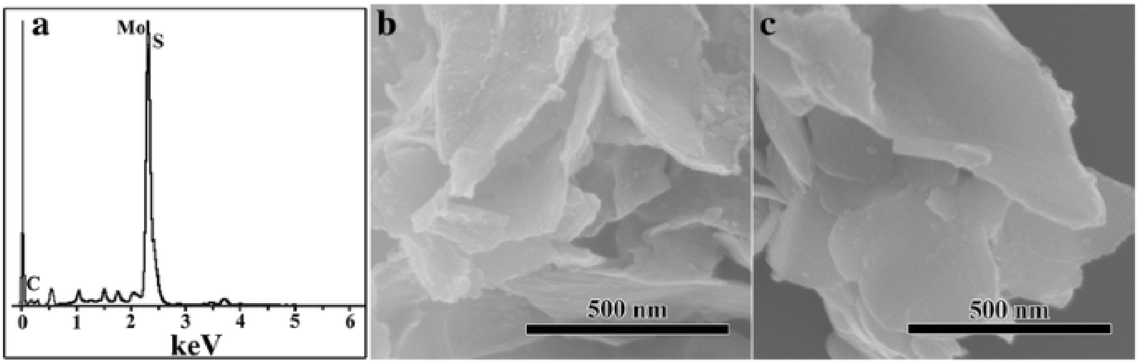

a EDX spectrum of MoS_2/C-700. **b**, **c** SEM images of MoS_2/C-700 nanocomposite

Full size image

Fig. 4

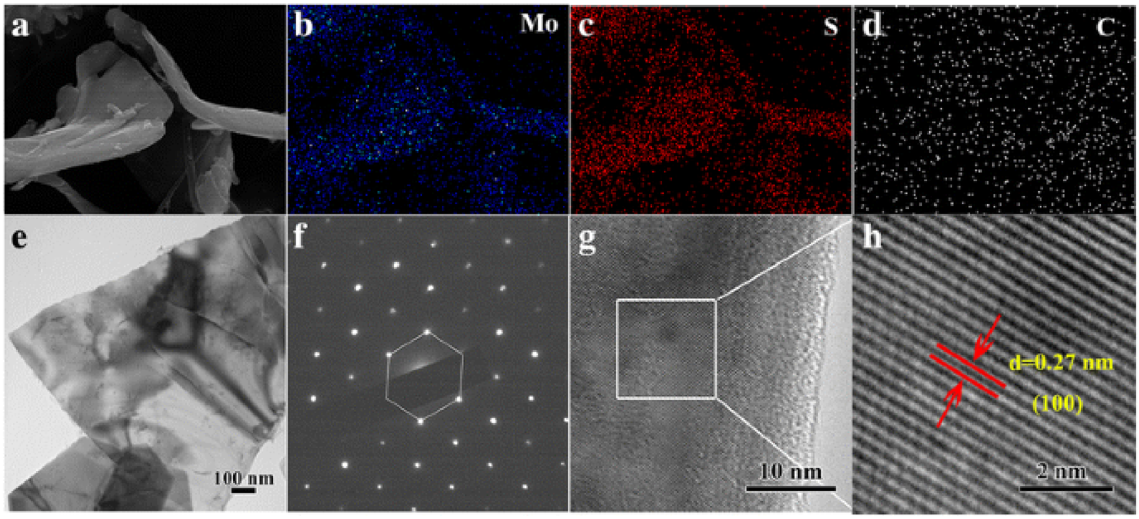

a–**d** Elemental mapping images of MoS_2/C-700; (**e**) TEM image, (**f**) the SAED and (**g**) High resolution TEM image of MoS_2/C-700 nanocomposite, (**h**) Enlarged HR-TEM image of the marked area in figure (**g**)

Full size image

As displayed in Fig. 4e–h, the morphology and structure of the as-synthesized MoS_2/C nanocomposites were investigated by transmission electron microscopy (TEM), selected area electron diffraction (SAED), and high-resolution transmission electron microscopy (HRTEM). The TEM image (Fig. 4e) and the SEM images (Fig. 3b, c) clearly show that the structure of MoS_2/C-700 nanocomposite is wrinkled two-dimensional nanosheets with the width of ~ 800 nm and the thickness of ~ 20 nm. SAED pattern in Fig. 4f shows that the hexagonal lattice structure of MoS_2 is well crystallized. Furthermore, the crystal lattices of the sample were shown at HRTEM profiles ((Fig. 4g, h) and Additional file 1: Figure S2). The profiles showed highly crystalline MoS_2 nanosheets with an interlayer distance of 0.27 nm corresponding to (100) plane of hexagonal MoS_2 [24, 34]. In addition, Additional file 1: Figure S2 clearly reveals that the carbon nanosheets were decorated with MoS_2 nanosheets.

Figure 5a shows the CV curves of the first 3 cycles of MoS_2/C-700 electrode at a scan rate of 0.1 mV s^{-1} in the potential window of 0.01–3.00 V vs. Li^+/Li. During the first cycle, the reduction peak at 1.0 V indicates the lithium insertion mechanism, which is due to the insertion of lithium ions into the MoS_2 layers to form Li_xMoS_2. At the same time, there has been a phase transition from 2H (trigonal prismatic) to 1T (octahedral) [48]. Another reduction peak at 0.4 V is attributed to the conversion of Li_xMoS_2 into metallic Mo and Li_2S. The broad oxidation peak located at 2.35 V represents the deintercalation of Li_2S to S. During the subsequent cycles, the two cathodic peaks at 1.0 and 0.4 V disappear with appearance of three new peaks at 2.0, 1.2, and 0.3 V, indicating the reduction of MoS_2 and the conversion from S_8 to polysulfides and then to Li_2S [24].

Fig. 5

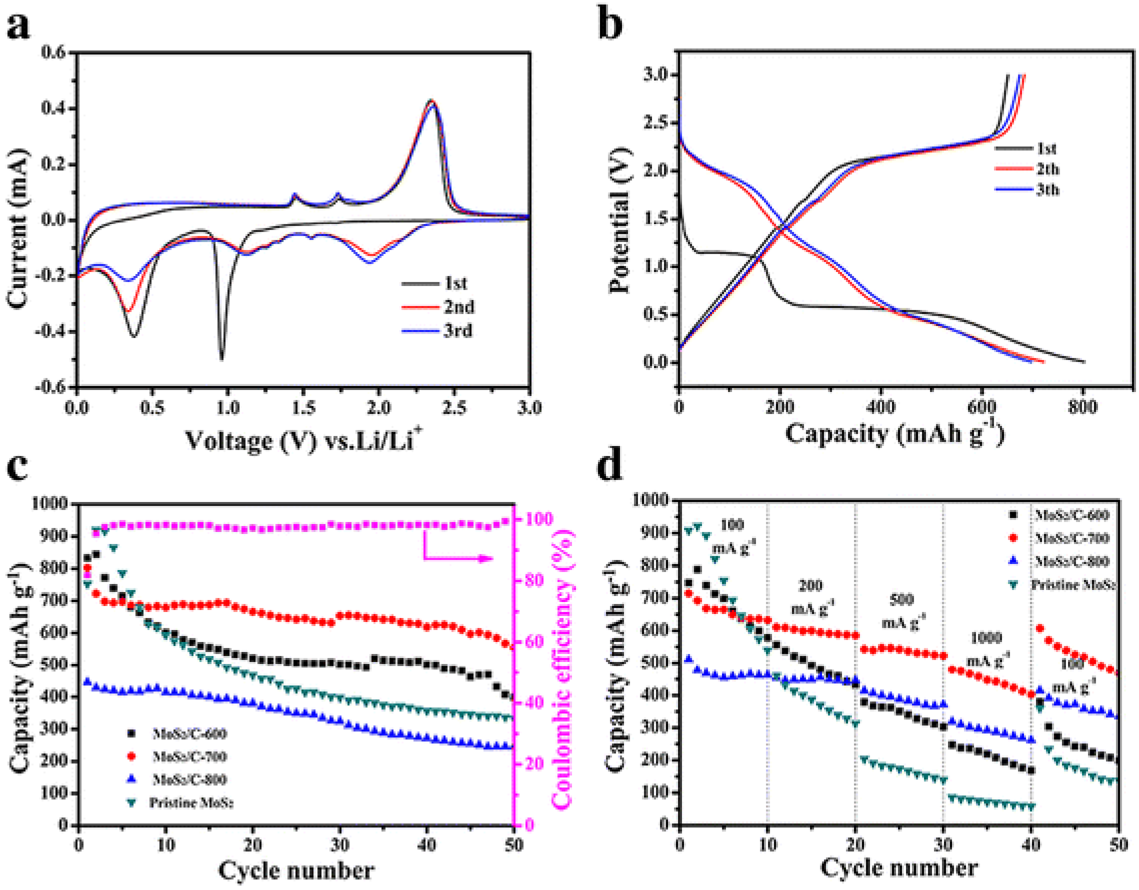

a CV curves of the first three cycles of MoS_2/C-700 electrode at a scan rate of 0.1 mV s^{-1}. **b** Discharge and charge curves of the first 3 cycles of MoS_2/C-700 electrode at a current density of 100 mA g^{-1}. **c** Cycling performance MoS_2/C electrode and the pristine MoS_2 electrode at a current density of 100 mA g^{-1}, and Coulombic efficiency of MoS_2/C-700 electrode. **d** Rate performance of MoS_2/C and the pristine MoS_2 electrode at the current densities ranging from 100 to 1000 mA g^{-1}

Full size image

The discharge and charge curves of the first 3 cycles of MoS_2/C-700 electrode were recorded, and the corresponding results were shown in Fig. 5b. In the first cycle, the discharge and charge capacities of MoS_2/C-700 electrode are 802.8 and 651.4 mAh g^{-1}, respectively, with a Coulomb efficiency of 81.14%. The irreversible capacity loss may be due to some irreversible reaction such as the decomposition of electrolyte and the formation of solid electrolyte interface (SEI) film [49, 50].

The cycle stability of whole MoS_2/C electrode and the pristine MoS_2 electrode at a current density of 100 mA g^{-1} are presented in Fig. 5c. At the same time, the Coulomb efficiency of MoS_2/C-700 is also recorded. After 50 cycles, the discharge capacities of MoS_2/C-600, MoS_2/C-700, MoS_2/C-800, and pristine MoS_2 electrode at a current density of 100 mA g^{-1} remain at 399.7, 554.9, 245.7, and 332.9 mAh g^{-1}, respectively. As shown in Additional file 1: Table S1, it has summarized the discharge capacities after 50 cycles of MoS_2-based electrode presented in other literature, the as-prepared MoS_2/C-700 display a comparable electrochemical performances compared to the previous work. It is concluded that the MoS_2/C-700 electrode shows the most outstanding cycle performance and the Coulomb efficiency of the sample maintained a high level at about 100% after the first 3 cycles. It may benefit from the small amount of graphitic carbon in this sample, leading to enhanced electrical conductivity of the nanocomposite.

In addition to the cycling stability, the high-rate performance is also an important factor for high-power applications. Figure 5d shows the rate performance of MoS_2/C and the pristine MoS_2 electrode at the current densities ranging from 100 to 1000 mA g^{-1}. At 1000 mA g^{-1}, the discharge capacity of MoS_2/C-700 can still maintain at a relatively high value of ~ 450 mAh g^{-1}, which is higher than the other MoS_2/C electrodes and pristine MoS_2 electrode we have prepared at the same current density. When the current density is changed back to 100 mA g^{-1}, the capacity of MoS_2/C-700 sample can recover up to ~ 500 mAh g^{-1} after 50 cycles at different current densities, revealing the good rate capability of the sample.

The electrochemical impedance spectra (EIS) measurements on the MoS_2/C and the pristine MoS_2 electrode were conducted in order to gain a further understanding about the excellent electrochemical performance of the MoS_2/C-700 sample (Fig. 6). There is a semicircle at the high frequency region followed by a slope line at the low frequency region on these Nyquist plots. It can be seen that the semicircle at the high frequency region of the MoS_2/C-700 sample is evidently smaller than that of the other three samples, which is related with the charge transfer resistance (R_{ct}) occurred at the electrolyte and electrodes interfaces. Therefore, this result further implies that the incorporation of potassium humate markedly improve the conductivity of MoS_2, leading to further improvement in the electrochemical performances.

Fig. 6

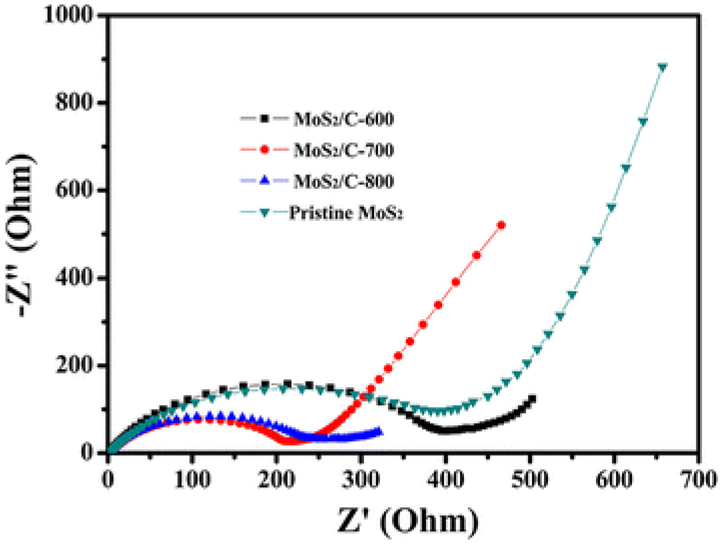

Nyquist plots of the MoS_2/C electrode and the pristine MoS_2 electrode tested in a frequency range of 0.01 Hz to 100 kHz

Full size image

Conclusions

In this work, two-dimensional MoS_2/C nanosheets were successfully synthesized via a co-precipitation/calcination route by employing an organic matter (potassium humate) and an inorganic substance ($(NH_4)_6Mo_7O_{24}$) as reagents. Structural characterizations show that as-prepared MoS_2/C-700 nanocomposite is two-dimensional (2D) MoS_2/C nanosheets with irregular shape. The 2D MoS_2/C nanosheets exhibited improved electrochemical performance when fabricated as anode material for LIBs. Furthermore, a possible reaction process was proposed. The current synthesis strategy may be expanded into the synthesis of other nanocomposite that can be served as anode materials for high-performance lithium-ion batteries.

Abbreviations

2D:

Two-dimensional

CV:

Cyclic voltammetry

DEC:

Diethyl carbonate (DEC)

DMC:

Dimethyl carbonate

EC:

Ethylene carbonate

EDX:

Energy-dispersive X-ray spectrometer

EIS:

Electrochemical impendence spectroscopy

FT-IR:

Fourier transform spectrophotometer

HRTEM:

High-resolution transmission electron microscopy

I_D:

The intensity of D-band

I_G:

The intensity of G-band

LIBs:

Lithium ion batteries

Mo-HA:

The precursors

MoS_2/C:

MoS_2/carbon

MoS_2/C-600:

MoS_2/C nanocomposite calcinated at 600 °C

MoS_2/C-700:

MoS_2/C nanocomposite calcinated at 700 °C

MoS_2/C-800:

MoS_2/C nanocomposite calcinated at 800 °C

NMP:

N-methyl-2-pyrrolidinone

PVDF:

Polyvinylidene fluoride

R_{ct}:

Charge transfer resistance

SEM:

Scanning electron microscope

TEM:

Transmission electron microscopy

TGA:

Thermogravimetric analyses

XRD:

X-ray diffraction

References

1. 1.

Wang J, Yang N, Tang H, Dong Z, Jin Q, Yang M, Kisailus D, Zhao H, Tang Z, Wang D (2013) Accurate control of multishelled Co_3O_4 hollow microspheres as high-performance anode materials in lithium-ion batteries. Angew Chem Int Ed 52:6417–6420

Article Google Scholar

2. 2.

Zou Y, Hu X, Ma H, Li SE (2015) Combined state of charge and state of health estimation over lithium-ion battery cell cycle lifespan for electric vehicles. J Power Sources 273:793–803

Article Google Scholar

3. 3.

Wu C, Tong X, Ai Y, Liu D-S, Yu P, Wu J, Wang ZM (2018) A review: enhanced anodes of Li/Na-ion batteries based on yolk-shell structured nanomaterials. Nano-Micro Lett 10:40

4. 4.

Armand M, Tarascon JM (2008) Building better batteries. Nature 451:652–657

Article Google Scholar

5. 5.

Kang B, Ceder G (2009) Battery materials for ultrafast charging and discharging. Nature 458:190–193

Article Google Scholar

6. 6.

Xin T, Feng L, Jiang W, Wang ZM (2016) High performance perovskite solar cells. Adv Sci 3:18742–18745

Google Scholar

7. 7.

Xie J, Liu L, Xia J, Zhang Y, Li M, Ouyang Y, Nie S, Wang X (2018) Template-free synthesis of Sb_2S_3 hollow microspheres as anode materials for Lithium-ion and sodium-ion batteries. Nano-Micro Lett. 10:12

Article Google Scholar

8. 8.

Cao X, Shi Y, Shi W, Rui X, Yan Q, Kong J, Zhang H (2013) Preparation of MoS_2-coated three-dimensional graphene networks for high-performance anode material in lithium-ion batteries. Small 9:3433–3438

Article Google Scholar

9. 9.

Kamali AR (2016) Eco-friendly production of high quality low cost graphene and its application in lithium ion batteries. Green Chem 18:1952–1964

Article Google Scholar

10. 10.

Xing X, Yu GH, Liu N, Bao ZN, Criddle CS, Yi C (2012) Graphene-sponges as high-performance low-cost anodes for microbial fuel cells. Energy Environ Sci 5:6862–6866

Article Google Scholar

11. 11.

Luo R, Lv W, Wen K, He W (2018) Overview of graphene as anode in lithium-ion batteries. J Electron Sci Technol 16:57-68

12. 12.

Li HH, Yabuuchi N, Meng YS, Kumar S, Breger J, Grey CP, Yang SH (2007) Changes in the cation ordering of layered O3 $Li_xNi_{0.5}Mn_{0.5}O_2$ during electrochemical cycling to high voltages: an electron diffraction study. Chem Mater 19:2551–2565

Article Google Scholar

13. 13.

Mn O, Vl C (2014) Alloy negative electrodes for Li-ion batteries. Chem Rev 114:11444–11502

Article Google Scholar

14. 14.

Reddy MV, Subba Rao GV, Chowdari BV (2013) Metal oxides and oxysalts as anode materials for li ion batteries. Chem Rev 113:5364

Article Google Scholar

15. 15.

Xu X, Liu W, Kim Y, Cho J (2014) Nanostructured transition metal sulfides for lithium ion batteries: progress and challenges. Nano Today 9:604–630

Article Google Scholar

16. 16.

Han F, Li WC, Li D, Lu AH (2014) In situ electrochemical generation of mesostructured Cu_2S/C composite for enhanced lithium storage: mechanism and material properties. Chem Aust 1:733–740

Google Scholar

17. 17.

Feng C, Huang L, Guo Z, Liu H (2007) Synthesis of tungsten disulfide (WS_2) nanoflakes for lithium ion battery application. Electrochem Commun 9:119–122

Article Google Scholar

18. 18.

Pham-Cong CJH, Yun J, Bandarenka AS, Kim J, Braun PV, Jeong SY, Cho CR (2016) Synergistically enhanced electrochemical performance of hierarchical $MoS_2/TiNb_2O_7$ hetero-nanostructures as anode materials for li-ion batteries. ACS Nano 11:1026–1033

Article Google Scholar

19. 19.

Tong X, Ashalley E, Lin F, Li H, Wang ZM (2015) Advances in MoS_2-based field effect transistors (FETs). Nano-Micro Lett. 7:203–218

Article Google Scholar

20. 20.

Perkgoz NK, Bay M (2016) Investigation of single-wall MoS_2 monolayer flakes grown by chemical vapor deposition. Nano-Micro Lett 8:70–79

Article Google Scholar

21.21.

Hwang H, Kim H, Cho J (2011) MoS_2 Nanoplates consisting of disordered graphene-like layers for high rate lithium battery anode materials. Nano Lett 11:4826

Article Google Scholar

22. 22.

Jiang L, Lin B, Li X, Song X, Xia H, Li L, Zeng H (2016) Monolayer MoS_2-graphene hybrid aerogels with controllable porosity for lithium-ion batteries with high reversible capacity. ACS Appl Mater Interfaces 8:2680–2687

Article Google Scholar

23. 23.

Kong D, He H, Song Q, Wang B, Lv W, Yang Q, Zhi L (2014) Rational design of MoS_2@graphene nanocables: towards high performance electrode materials for lithium ion batteries. Energy Environ Sci 7:3320–3325

Article Google Scholar

24. 24.

Zhou J, Qin J, Zhang X, Shi C, Liu E, Zhao N, He C (2015) 2D space-confined synthesis of few-layer MoS_2 anchored on carbon nanosheet for lithium-ion battery anode. ACS Nano 9:3837

Article Google Scholar

25. 25.

Zhang S, Chowdari BV, Wen Z, Jin J, Yang J (2015) Constructing highly oriented configuration by few-layer MoS_2: toward high-performance lithium-ion batteries and hydrogen evolution reactions. ACS Nano 9:12464–12472

Article Google Scholar

26. 26.

Li J, Hou Y, Gao X, Guan D, Xie Y, Chen J, Yuan C (2015) A three-dimensionally interconnected carbon nanotube/layered MoS_2 nanohybrid network for lithium ion battery anode with superior rate capacity and long-cycle-life. Nano Energy 16:10–18

Article Google Scholar

27.27.

Huang X, Zeng Z, Zhang H (2013) Metal dichalcogenide nanosheets: preparation, properties and applications. Chem Soc Rev 42:1934

Article Google Scholar

28. 28.

Liu J, Fu A, Wang Y, Guo P, Feng H, Li H, Zhao XS (2017) Spraying coagulation-assisted hydrothermal synthesis of MoS_2/carbon/graphene composite microspheres for lithium-ion battery applications. ChemElectroChem 4:2027-2036

29. 29.

Deng Z, Jiang H, Hu Y, Liu Y, Zhang L, Liu H, Li C (2017) 3D ordered macroporous MoS_2@C nanostructure for flexible Li-ion batteries. Adv Mater 9:1603020

30. 30.

Zhao Z, Qin F, Kasiraju S, Xie L, Alam MK, Chen S, Wang D, Ren Z, Wang Z, Grabow LC (2017) Vertically aligned MoS_2/Mo_2C hybrid nanosheets grown on carbon paper for efficient electrocatalytic hydrogen evolution. ACS Catal 7:7312–7318

Article Google Scholar

31.31.

Chang K, Chen W (2011) L-cysteine-assisted synthesis of layered MoS_2/graphene composites with excellent electrochemical performances for lithium ion batteries. ACS Nano 5:4720–4728

Article Google Scholar

32. 32.

Shyyko LO, Kotsyubynsky VO, Budzulyak IM, Sagan P (2016) MoS_2/C multilayer nanospheres as an electrode base for lithium power sources. Nanoscale Res Lett 11:243

Article Google Scholar

33. 33.

Wang J-Z, Lu L, Lotya M, Coleman JN, Chou S-L, Liu H-K, Minett AI, Chen J (2013) Development of MoS_2-CNT composite thin film from layered MoS_2 for lithium batteries. Adv Energy Mater 3:798–805

Article Google Scholar

34. 34.

Fu W, Du FH, Su J, Li XH, Wei X, Ye TN, Wang KX, Chen JS (2014) In situ catalytic growth of large-area multilayered graphene/MoS_2 heterostructures. Sci Rep 4:4673

Article Google Scholar

35. 35.

Zhang X, Zhao R, Wu Q, Li W, Shen C, Ni L, Yan H, Diao G, Chen M (2017) Petal-like MoS_2 Nanosheets space-confined in hollow mesoporous carbon spheres for enhanced Lithium storage performance. ACS Nano 11:8429-8436

36. 36.

Beshkar F, Zinatloo-Ajabshir S, Salavati-Niasari M (2015) Simple morphology-controlled fabrication of nickel chromite nanostructures via a novel route. Chem Eng J 279:605–614

Article Google Scholar

37. 37.

Vattikuti SVP, Chan B, Reddy CV, Shim J, Venkatesh B (2015) Co-precipitation synthesis and characterization of faceted MoS_2 nanorods with controllable morphologies. Appl Phys A Mater Sci Process 119:813–823

Article Google Scholar

38. 38.

Huang G, Liu Q, Kang W, Xing B, Chen L, Zhang C (2016) Potassium humate based reduced graphite oxide materials for supercapacitor applications. Electrochim Acta 196:450–456

Article Google Scholar

39. 39.

Luo HM, Yang YF, Chen YZ, Zhang JQ, Zhao X (2015) Structure and electrochemical performance of highly porous carbons by single-step potassium humate carbonization for application in supercapacitors. J Appl Electrochem 46:1–9

Google Scholar

40. 40.

Wang Z, Chen T, Chen W, Chang K, Ma L, Huang G, Chen D, Lee JY (2013) CTAB-assisted synthesis of single-layer MoS_2-graphene composites as anode materials of li-ion batteries. J Mater Chem A 1:2202–2210

Article Google Scholar

41.41.

Choi M, Hwang J, Setiadi H, Chang W, Kim J (2017) One-pot synthesis of molybdenum disulfide-reduced graphene oxide (MoS_2-RGO) composites and their high electrochemical performance as an anode in lithium ion batteries. J Supercrit Fluids 127:81–89

Article Google Scholar

42. 42.

Yang W, He L, Tian X, Yan M, Yuan H, Liao X, Meng J, Hao Z, Mai L (2017) Carbon-MEMS-based alternating stacked MoS_2@rGO-CNT micro-supercapacitor with high capacitance and energy density. Small 13:1700639

43. 43.

Liu Y, Ghosh R, Wu D, Ismach A, Ruoff R, Lai K (2014) Mesoscale imperfections in MoS_2 atomic layers grown by a vapor transport technique. Nano Lett 14:4682

Article Google Scholar

44. 44.

Zhao X, Hu C, Cao M (2013) Three-dimensional MoS_2 hierarchical nanoarchitectures anchored into a carbon layer as graphene analogues with improved lithium ion storage performance. Chem Asian J 8:2701–2707

Article Google Scholar

45. 45.

Jiang Y, Li X, Yu S, Jia L, Zhao X, Wang C (2015) Reduced graphene oxide-modified carbon nanotube/polyimide film supported MoS_2 nanoparticles for electrocatalytic hydrogen evolution. Adv Funct Mater 25:2693–2700

Article Google Scholar

46. 46.

Zhao S, Jin R, Song Y, Zhang H, House SD, Yang JC, Jin R (2017) Atomically precise gold nanoclusters accelerate hydrogen evolution over MoS_2 nanosheets: the dual interfacial effect. Small 13:1701519

47. 47.

Wang J, Luo C, Gao T, Langrock A, Mignerey AC, Wang C (2015) An advanced MoS_2/carbon anode for high-performance sodium-ion batteries. Small 11:473–481

Article Google Scholar

48. 48.

Fang X, Yu X, Liao S, Shi Y, Hu YS, Wang Z, Stucky GD, Chen L (2012) Lithium storage performance in ordered mesoporous MoS_2 electrode material. Microporous Mesoporous Mater 151:418–423

Article Google Scholar

49. 49.

Chang K, Chen W (2011) Single-layer MoS_2/graphene dispersed in amorphous carbon: towards high electrochemical performances in rechargeable lithium ion batteries. J Mater Chem 21:17175–17184

Article Google Scholar

50. 50.

Du G, Guo Z, Wang S, Zeng R, Chen Z, Liu H (2010) Superior stability and high capacity of restacked molybdenum disulfide as anode material for lithium ion batteries. Chem Commun 46:1106–1108

Article Google Scholar

Download references

Acknowledgements

The authors gratefully acknowledge the financial support given for this work by the National Natural Science Foundation of China, International Cooperation Project of Xinjiang Science and Technology Bureau, the Project of Xinjiang Education Office and National Program on Key Basic Research Project (973 Program).

Funding

This work was supported by the National Natural Science Foundation of China (U1503391, 51564045, 21566037, and 51272038), International Cooperation Project of Xinjiang Science and Technology Bureau (2017E0116 and 2017E01005), the Project of Xinjiang Education Office (XJEDU2017I004), and National Program on Key Basic Research Project (973 Program) 2013CB933301.

Availability of data and materials

The datasets supporting the conclusions of this article are included within the article and its additional files.

Author information

Affiliations

1. **Institute of Fundamental and Frontier Science, University of Electronic Science and Technology of China, Chengdu, 610054, People's Republic of China**
   Qin Geng, Xin Tong, Gideon Evans Wenya & Zhiming M. Wang

2. **Ministry Key Laboratory of Oil and Gas Fine Chemicals, College of Chemistry and Chemical Engineering, Xinjiang University, Urumqi, 830046, People's Republic of China**
   Qin Geng, Chao Yang, Jide Wang & Xintai Su

3. **Moscow State Mining University, Moscow, 109807, Russia**
   A. S. Maloletnev

Contributions

QG prepared the manuscript and carried out the experiment. XT, GEW, CY, ASM and JW helped in the technical support for the characterizations. XS and ZMW designed the experiment. All the authors discussed the results and approved the final manuscript.

Corresponding authors

Correspondence to Zhiming M. Wang or Xintai Su.

Ethics declarations

Competing interests

The authors declare that they have no competing interests.

Publisher’s Note

Springer Nature remains neutral with regard to jurisdictional claims in published maps and institutional affiliations.

Additional file

Additional file 1: of Humate-assisted Synthesis of MoS2/C Nanocomposites via Co-Precipitation/Calcination Route for High Performance Lithium Ion Batteries

Skip to file navigationSkip to generic navigation

sorry, we can't preview this file

figshare

Download

Additional File 1

Equations 1â “5. The proposed reactions for the synthesis of MoS2. Table S1. The composition analysis of potassium humate. Figure S1. SEM images of (a) MoS2/C-600 and (b) MoS2/C-800 nanocomposite. Figure S2. High-resolution TEM image of MoS2/C-700 nanocomposite. Table S2. Comparison of electrochemical performance of MoS2-based electrodes. (DOC 2203Â kb)

Additional file 1:

Equations 1–5. The proposed reactions for the synthesis of MoS_2. **Table S1.** The composition analysis of potassium humate. **Figure S1.** SEM images of (a) MoS_2/C-600 and (b) MoS_2/C-800 nanocomposite. **Figure S2.** High-resolution TEM image of MoS_2/C-700 nanocomposite. **Table S2.** Comparison of electrochemical performance of MoS_2-based electrodes. (DOC 2203 kb)

Rights and permissions

Open Access This article is distributed under the terms of the Creative Commons Attribution 4.0 International License (http://creativecommons.org/licenses/by/4.0/), which permits unrestricted use, distribution, and reproduction in any medium, provided you give appropriate credit to the original author(s) and the source, provide a link to the Creative Commons license, and indicate if changes were made.